

1 The authors have addressed most of my comments. However, I still have some questions about the calibration
2 curve (specific comment L181).

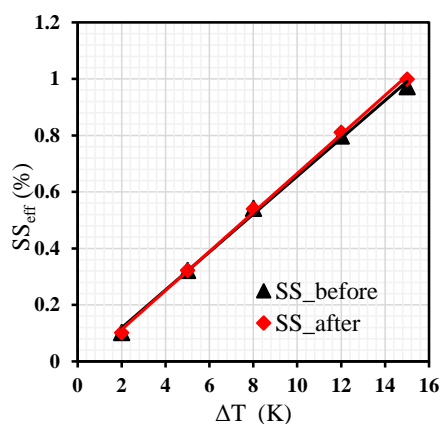
3 In the response the authors tried to explain the calibration procedure but did not answer my questions directly. I've
4 been a user of CCN counter since 8 years and I know how to calibrate it, but I am still a bit confused.

5 In the last response, the authors wrote "We didn't change the corresponding parameters to SS although we
6 calibrated it before the campaign". I am wondering why the authors did not apply the new calibration curve. It
7 means an older curve was used to convert the set SS to delfTs, and these delfTs were used to calculate the corrected
8 SS, right? Can you add also the older calibration curve into the figure?

9 Re: We are sorry that our response confused the reviewer. Actually, our meaning is that we did not change the set
10 parameters (Temp Gradient Slope and Temp Gradient Intercept) in the "CCN Calibration Editor.vi" software
11 before the campaign. New linear curves between effective supersaturation (SS_{eff}) and ΔT were established before
12 and after the campaign (Fig. 1) and their mean curve was used in this study. There is a one-to-one correspondence
13 between the set SS and the set ΔT . We calculated the corrected SS utilizing the new curve and the set ΔT . Therefore,
14 the corrected SS (0.11, 0.13, 0.22, 0.40, and 0.75%) were different with the set SS (0.07, 0.1, 0.2, 0.4, and 0.8%).
15 The corrected SS were used in this study. Same calibrating procedures were reported by Deng et al. (2011) and
16 Zhang et al. (2014).

17 We are sorry we cannot show the older calibration curve because we can't find the old data. We never used
18 the older curve in this study. There was a small difference for the relationship between SS_{eff} and ΔT before and
19 after this campaign (Fig. 1), suggesting the new curve was reliable and the CCNc worked well during this
20 campaign.

21



22

23 Figure 1. The results of SS calibration experiments with ammonium sulfate: CCN efficiency spectra measured at 5
24 different temperature gradient (ΔT). SS_{before} and SS_{after} are the calibration results before and after the
25 campaign respectively.

26

27 By the way, I am also very curious about how the author calibrated the temperature sensors in CCN counter. I think
28 this is not part of the standard calibration procedure which an user is supposed to do. Can you explain how you did
29 it?

30 Re: The user cannot do the temperature sensor calibration because it needs some special instruments. A technical
31 company help us do the calibration. The sensor performance can be adjusted through regulating resistance. The

32 engineer first puts CCNc in a thermostatic container, and then adjusts these resistors to make the sensor
33 temperatures consistent with the standard temperature inside the container.

34 **References**

36 Deng Z.Z., Ma N., Liu P.F., Xu W.Y., Zhao C.S., Ran L., Chen J., Liang Z., Liang S. and Huang M.Y.:
37 Size-resolved and bulk activation properties of aerosols in the North China Plain, Atmos. Chem. Phys., 11,
38 3835-3846, 2011.

39 Zhang F., Li Y., Li Z., Sun L., Li R., Zhao C., Wang P., Sun Y., Liu X., Li J., Li P., Ren G. and Fan T.: Aerosol
40 hygroscopicity and cloud condensation nuclei activity during the AC3Exp campaign: implications for cloud
41 condensation nuclei parameterization, Atmos. Chem. Phys., 14, 13423-13437, 10.5194/acp-14-13423-2014, 2014.

43 **Characterization of aerosol hygroscopicity, mixing state, and** 44 **CCN activity at a suburban site in the central North China Plain**

45

46 Yuying Wang¹, Zhanqing Li^{1,2}, Yingjie Zhang^{3,2}, Wei Du^{3,2,4}, Fang Zhang¹, Haobo Tan^{5,4},
47 Hanbing Xu^{6,5}, Tianyi Fan¹, Xiaoi Jin¹, Xinxin Fan¹, Zipeng Dong¹, Qiuyan Wang^{2,6}, Yele
48 Sun^{3,2,4,3}

49

50

51 ¹[State Key Laboratory of Earth Surface Processes and Resource Ecology](#), College of Global
52 Change and Earth System Science, Beijing Normal University, Beijing 100875, China

53 ²[Department of Atmospheric and Oceanic Sciences and ESSIC, University of Maryland, College](#)
54 [Park, Maryland, USA](#)

55 ^{3,2}State Key Laboratory of Atmospheric Boundary Layer Physics and Atmospheric Chemistry,
56 Institute of Atmospheric Physics, Chinese Academy of Sciences, Beijing 100029, China

57 ^{4,3}College of Earth Sciences, University of Chinese Academy of Sciences, Beijing 100049, China

带格式的: 上标

58 ⁵⁴Key Laboratory of Regional Numerical Weather Prediction, Institute of Tropical and Marine

59 Meteorology, China Meteorological Administration, Guangzhou 510080, China

60 ⁶⁵Shared Experimental Education Center, Sun Yat-sen University, Guangzhou 510275, China

61 ⁷⁶Collaborative Innovation Center on Forecast and Evaluation of Meteorological Disasters,

62 Nanjing University of Information Science and Technology, Nanjing, 210044, China

63

64 **Correspondence to: Zhanqing Li (zli@atmos.umd.edu)*

65

66 **Abstract**

67

68 This study investigates aerosol hygroscopicity, mixing state, and cloud condensation
69 nucleation as part of the Atmosphere-Aerosol-Boundary Layer-Cloud Interaction Joint
70 Experiment done in the summer of 2016 at Xingtai (XT), a suburban site located in
71 the center of the North China Plain (NCP). In general, the probability density function
72 (PDF) of the hygroscopicity parameter (κ) for 40–200-nm particles had a unimodal
73 distribution, and mean κ -PDF patterns for different sizes were similar, suggesting that
74 the particles were highly aged and internally mixed because of strong photochemical
75 reactions. The κ calculated from the hygroscopic growth factor in the daytime and at
76 night suggests that photochemical reactions largely enhanced the aerosol
77 hygroscopicity. This effect became weaker as the particle size increased. In addition,
78 the aerosol hygroscopicity was much larger at XT than at other sites in the NCP. This
79 is because new particle formation takes place much more frequently in the central
80 NCP, which is heavily polluted from industrial activities, than elsewhere in the region.

81 The evolution of the planetary boundary layer played a dominant role in dictating
82 aerosol mass concentration. Particle size was the most important factor influencing
83 the ability of aerosols to activate, whereas the effect of chemical composition was
84 secondary, especially when supersaturation was high. Using a fixed value of $\kappa =$
85 0.31 to calculate the cloud condensation nuclei number concentration in this region
86 suffices.

87 **1. Introduction**

88 Aerosols, defined as the mixture of solid and liquid particles suspended in air, are
89 ubiquitous in the atmosphere because of direct emissions from biogenic and
90 anthropogenic sources, and the secondary transformation from gas precursors. Aerosol
91 particles play an important role in climate change through direct and indirect effects
92 (e.g., Ramanathan et al., 2001; Rosenfeld et al., 2008; Li et al., 2016). However, the
93 impact of aerosols on climate change is difficult to simulate because of the highly
94 variable physical and chemical properties of aerosols, and complex aerosol-cloud
95 interactions (IPCC, 2013; Lebo et al., 2017).

96 The hygroscopic growth and mixing state of aerosol particles are important for
97 estimating the direct radiative effect of aerosols on Earth's climate. This is because
98 the growth and mixing can change the particle size and optical properties of aerosol
99 particles which influences the solar radiation budget and atmospheric visibility. In
100 addition, aerosol particles can be activated as cloud condensation nuclei (CCN) under
101 supersaturation (SS) conditions. The variability in CCN number concentration (N_{CCN})

102 can modify both cloud microphysical properties (Twomey, 1974; Albrecht, 1989) and
103 morphology (Rosenfeld et al., 2008) and can lead to a broad impact on a wide range
104 of meteorological variables including severe weather events (Li et al., 2017a).

105 Previous studies have addressed three main aerosol properties influencing the
106 CCN activation, namely, particle size, chemical composition, and mixing state.
107 However, their relative importance is different under different environmental
108 conditions (e.g., Dusek et al., 2006; Ervens et al., 2007; Cubison et al., 2008; Deng et
109 al., 2011; Zhang et al., 2014; Schmale et al., 2018).

110 Ambient aerosols are composed of different species, including inorganic ions,
111 organic components, black carbon (BC), and mineral dust. Inorganics mainly contain
112 sulfate, nitrate, and ammonium, while organic aerosols (OA) consist of thousands of
113 chemicals (Jacobson et al., 2000). The hygroscopicity and CCN activity of a single
114 component can be characterized according to laboratory studies (e.g., Petters and
115 Kreidenweis, 2007), but the properties of their mixtures are hard to estimate because
116 of the different chemical species and mixing states of particles in the atmosphere.
117 Therefore, aerosol hygroscopicity and CCN activity are very different in different
118 regions due to different chemical compositions. Comprehensive field measurements
119 of aerosol properties in different regions are thus necessary to improve models.

120 China, especially the North China Plain (NCP), has been suffering from severe air
121 pollution over the last couple of decades due to rapid industrialization and
122 urbanization. Diverse sources and aging processes make aerosol properties
123 particularly diverse and complex in this part of the world. As such, the region has

124 drawn much attention regarding the aerosol mixing state, hygroscopicity, and CCN
125 activity (Deng et al., 2011; Liu et al., 2011; Zhang et al., 2014; F. Zhang et al., 2016;
126 S.L. Zhang et al., 2016; Wu et al., 2016; Y. Wang et al., 2017). Liu et al. (2011) and
127 Y. Wang et al. (2017) have suggested that ambient particles are mostly an external
128 mixture with different hygroscopicities. Deng et al. (2011) have shown that the
129 aerosol number size distribution is critical in the prediction of N_{CCN} while Zhang et al.
130 (2014, 2017) have highlighted the importance of chemical composition in determining
131 particle activation properties. However, these studies were done using data from the
132 northern part of the NCP. Few studies have focused on the central region of the NCP.
133 Compared to the northern part of the NCP, the central part of the NCP is more affected
134 by industrial emissions because a dense cluster of China's heavy industries exists
135 there (Fu et al., 2014). Measurements of aerosol properties in the central part of the
136 NCP are thus critically needed to investigate the impact of air pollution on the
137 environment and climate change.

138 Xingtai (XT), a city located in the center of the NCP, is considered one of the
139 most polluted cities in China. Local industrial and domestic sources of pollution are
140 the greatest contributors to severe haze events in that region (Wang et al., 2014). A
141 field experiment called the Atmosphere-Aerosol-Boundary Layer-Cloud (A²BC)
142 Interaction Joint Experiment was done at a suburban site in XT in the summer of 2016.
143 Differences in aerosol properties at this site and at sites in the northern part of the
144 NCP were found.

145 The paper is organized as follows. Sections 2 and 3 describe the measurement

146 method and data analysis theory. Section 4 presents and discusses the measurement
147 results, which includes data time series, aerosol mixing state, hygroscopicity, CCN
148 prediction and its sensitivity to chemical composition. A summary and conclusions are
149 given in section 5.

150 **2. Measurements**

151 **2.1. Sampling site and meteorology**

152 The A²BC experiment was done at the National Meteorological Basic Station
153 located in XT (37.18°N, 114.37°E, 180 m above sea level) from 1 May to 15 June of
154 2016. This suburban site is situated ~17 km northwest of the XT urban area in
155 southern Hebei Province, which is located in the central part of the NCP and to the
156 east of the Taihang Mountains (Fig. 1a). This region is heavily populated, urbanized,
157 and industrialized. Major industrial manufacturers include coal-based power plants,
158 steel and iron works, glassworks, and cement mills. Weak diffusion conditions and
159 heavy industrial emissions lead to exceptionally high concentrations of particulate
160 matter (PM) with diameters less than 10 μm and 2.5 μm (PM_{2.5}), as well as gas
161 pollutants such as sulfur dioxide (SO₂), volatile organic compounds (VOCs), and
162 nitrogen oxides (NO_x) during the frequently occurring haze episodes in this region
163 (Wang et al., 2014; Fu et al., 2014). Figure 1b shows the mean distribution of SO₂
164 concentrations from May of 2012 to 2016 which confirms that the measurement site is
165 located in one of the pollution centers in this region. A detailed analysis of gas
166 precursors and aerosol chemical species shows that this station is a representative site

167 in this region (Zhang et al., 2018).

168 Time series of meteorological variables measured at this meteorological station
169 are shown in Fig. S1. This site is strongly affected by mountain-valley winds.
170 Southeasterly winds prevail during the day and at night northwesterly winds prevail
171 (Fig. S1 and Fig. S2). There was almost no precipitation during the study period. The
172 ambient temperature (T) and relative humidity (RH) time series show opposing trends.
173 Campaign-mean values of T and RH are 21.9°C and 51.6%, respectively.

174 **2.2. Instrumentation and operation**

175 **2.2.1. Aerosol hygroscopicity measurements**

176 The custom-built hygroscopicity tandem differential mobility analyzer (HTDMA)
177 used in this study has been described in detail by others (Tan et al., 2013; Y. Wang et
178 al., 2017). Briefly, ambient aerosols are first dried and neutralized by a Nafion dryer
179 and a soft X-ray charger. A differential mobility analyzer (DMA₁, model 3081L, TSI
180 Inc.) is used to select monodispersed particles of a certain diameter. The
181 monodispersed particles are then passed through a Nafion humidifier with a controlled
182 higher RH and are humidified. A second DMA (DMA₂, same model as the DMA₁)
183 and a water-based condensation particle counter (WCPC, model 3787, TSI Inc.) are
184 used to measure the number size distribution of the humidified particles. The DMA₁
185 and WCPC can also be connected directly to measure the 10–400-nm particle number
186 size distribution (PNSD). In this study, the dry diameters selected by the DMA₁ were
187 40, 80, 110, 150, and 200 nm, and the humidified RH was set to 85%. The RH

188 calibration with ammonium sulfate for the H-TDMA is shown in Fig. S3.

189 The hygroscopic growth factor (GF) is defined as the ratio of the humidified
190 diameter at a given RH to the dry diameter:

$$191 \quad \text{GF} = \frac{D_p(\text{RH})}{D_{p0}}, \quad (1)$$

192 where $D_p(\text{RH})$ is the particle diameter at the given RH and D_{p0} is the dry diameter
193 selected by the DMA₁. The measured distribution function versus GF can be
194 calculated with WCPC data downstream from the DMA₁ and DMA₂. The GF
195 probability density function is then retrieved using the TDMAFIT algorithm
196 (Stolzenburg and McMurry, 1988, 2008).

197 **2.2.2. Aerosol chemical composition measurements**

198 An Aerosol Chemical Speciation Monitor (ACSM) was used to measure
199 non-refractory submicron aerosol species (sulfate, nitrate, ammonium, chloride, and
200 organics) in real-time. A PM_{2.5} URG cyclone (model URG-2000-30ED) was installed
201 in the front of the sampling inlet to remove coarse particles (> 2.5 μm in diameter).
202 Before sampling into the ACSM, aerosol particles were dried (below 40% RH) by a
203 silica gel diffusion dryer. The ACSM was calibrated routinely with pure ammonium
204 nitrate to determine its ionization efficiency. More detailed descriptions about the
205 ACSM are given by Ng et al. (2011) and Sun et al. (2012). A positive matrix factor
206 analysis was used to analyze the organic spectral matrices according to Ulbrich et al.
207 (2009). Three factors, i.e., hydrocarbon-like OA (HOA), cooking OA (COA), and
208 oxygenated OA (OOA), are chosen as the ACSM dataset. HOA and COA are both

209 primary organic aerosols (POA) while OOA is the secondary organic aerosol (SOA).

210 The ACSM does not detect refractory material such as BC, so a seven-wavelength
211 aethalometer (AE-33, Magee Scientific Corp.) with a PM with diameters less than 1
212 μm (PM_{10}) cyclone was used to measure the BC mass concentration of BC particles
213 with diameters $< 1.0 \mu\text{m}$. Mineral dust and sea salt are the other refractory species, but
214 they typically exist in the coarse mode and contribute negligibly to PM_{10} (Juranyi et al.,
215 2010; Meng et al., 2014).

216 **2.2.3. Aerosol size distribution and CCN measurements**

217 The aerosol particle number size distribution (15–685 nm) was measured by a
218 scanning mobility particle sizer (SMPS) that was equipped with a long DMA (model
219 3081L, TSI Inc.) and a condensation particle counter (model 3775, TSI Inc.). A
220 single-column continuous-flow thermal-gradient cloud condensation nuclei counter
221 (model CCNC-100, DMT Inc.) was used to measure the bulk CCN number
222 concentration. Five SS levels, i.e., 0.07, 0.1, 0.2, 0.4, and 0.8%, were set in the CCNC
223 and the running time was 10 min for each SS level. The SS levels in the CCNC were
224 calibrated with pure ammonium sulfate (Rose et al., 2008) before and after the
225 measurement campaign. The corrected SS levels were 0.11, 0.13, 0.22, 0.40, and
226 0.75%.

227 The aerosol activation ratio (AR) at a certain SS is calculated as N_{CCN} divided by
228 the total particle number concentration in the 15–685-nm range ($N_{15-685 \text{ nm}}$), i.e., $\text{AR} =$
229 $N_{\text{CCN}} / N_{15-685 \text{ nm}}$. The SMPS does not measure particle number concentrations below

230 15 nm. Since the activation critical diameter is always larger than 15 nm at these SS
231 levels (Zhang et al., 2014), this does not affect the calculated N_{CCN} . Aerosol particles
232 with diameters greater than 685 nm are also not detected by the SMPS. These larger
233 particles will always act as CCN due to their larger dry sizes. Note that the number
234 concentration above 685 nm in the atmosphere is always negligible (Juranyi et al.,
235 2010).

236 **2.2.4. Other measurements**

237 In this study, a micro-pulse lidar (MPL-4B, Sigmaspace Corp.) was used to study
238 the evolution of the planetary boundary layer (PBL) which plays a crucial role in
239 modulating surface air quality (Z. Li et al., 2017b). The pulse repetition rate of the
240 MPL was 2.5 kHz at a visible wavelength of 532 nm. The peak value of the optical
241 energy of the laser beam was 8 μ J. The pulse duration ranged from 10 to 100 ns, and
242 the pulse interval was set to 200 ns, corresponding to a spatial resolution of 30 m. The
243 MPL-retrieved PBL height is the altitude where a sudden decrease in the scattering
244 coefficient occurs (Brooks, 2003; Quan et al., 2013). Trace gas analyzers
245 (manufactured by ECOTECH) were used to measure the gaseous species of ozone,
246 SO₂, NO_x, NO, and carbon monoxide. More detailed descriptions about the analyzers
247 are given by Zhu et al. (2016).

248 Two containers at ground level housed all sampling instruments. Two air
249 conditioners maintained the temperature at 20–25°C inside the containers. All
250 stainless tube inlets were ~1.5 m above the top of the containers.

251 3. Theory

252 3.1. Hygroscopicity parameter

253 To link hygroscopicity measurements below and above the water vapor saturation,
254 the Köhler theory (Köhler, 1936) is parameterized using the hygroscopicity parameter
255 κ (Petters and Kreidenweis, 2007). This is known as the κ -Köhler theory. According
256 to the theory, the equilibrium equation for a solution droplet at a saturation ratio $S(D)$
257 is

$$258 \quad S(D) = \frac{D^3 - D_d^3}{D^3 - D_d^3(1 - \kappa)} \exp\left(\frac{4\sigma_{s/a}M_w}{RT\rho_w D}\right) , \quad (2)$$

259 where D and D_d are the wet and dry droplet diameters, respectively, $\sigma_{s/a}$ is the
260 surface tension coefficient, M_w is the mole mass of water, R is the universal gas
261 constant, T is the temperature, and ρ_w is the density of water.

262 Below the water vapor saturation, $S(D)$ is RH, D is $D_p(\text{RH})$, and D_d is D_{p0}
263 from Eq. (1). The κ parameter is then calculated using H-TDMA data according to Eq.
264 (1) and Eq. (2):

$$265 \quad \kappa_{\text{gf}} = (\text{GF}^3 - 1) \cdot \left[\frac{1}{\text{RH}} \exp\left(\frac{4\sigma_{s/a}M_w}{RT\rho_w D_d \text{GF}}\right) - 1 \right] . \quad (3)$$

266 For a multicomponent particle, the Zdanovskii–Stokes–Robinson (ZSR) mixing
267 rule (Stokes and Robinson, 1966) can also estimate κ using chemical composition
268 data:

$$269 \quad \kappa_{\text{chem}} = \sum_i \varepsilon_i \kappa_i, \quad (4)$$

270 where ε_i and κ_i are the volume fraction and κ for the i th chemical component,
271 respectively. The ACSM provides the mass concentrations of inorganic ions and

272 organics. A simplified ion-pairing scheme such as that described by Gysel et al. (2007)
273 is applied to convert ion mass concentrations to mass concentrations of their
274 corresponding inorganic salts (see Table S1 in the supplement). Table S1 also lists κ
275 and the gravimetric density of each individual component under supersaturated
276 conditions. In the following discussions, κ_{gf} and κ_{chem} denote the hygroscopicity
277 parameters derived from H-TDMA measurements and estimated using the ZSR
278 mixing rule, respectively.

279 3.2. CCN estimation

280 The critical supersaturation (s_c , $s_c = S_c - 1$) for the D_d of a particle with
281 hygroscopicity κ is calculated from the maximum of the κ -Köhler curve (Eq. 2;
282 Petters and Kreidenweis, 2007). The D_d is also the critical diameter corresponding to
283 the s_c when κ is known. The s_c - D_d relationship can thus be established. According to
284 this relationship, the critical diameter ($D_{0,\text{crit}}$) can be calculated using the estimated
285 κ_{chem} (Eq. 4) at a given SS. All particles larger than $D_{0,\text{crit}}$ will activate as CCN,
286 assuming that aerosols are internally mixed. Then the CCN number concentration can
287 be estimated from the integral of the aerosol size distribution provided by the SMPS
288 from $D_{0,\text{crit}}$ to the maximum measured size (D_{max}):

$$289 N_{\text{CCN}}(\text{SS}) = \int_{D_{0,\text{crit}}(\text{SS})}^{D_{\text{max}}} \frac{dN(D)}{d\log(D)} d\log(D) . \quad (5)$$

290 $N_{\text{CCN}}(\text{SS})$ can then be compared to the number of CCN at the same SS measured by
291 the CCNC.

292 4. Results and discussion

293 4.1. Overview

294 Figures 2 and 3 show time series of the main aerosol properties measured during
295 the field campaign. The PNSD changes dramatically (Fig. 2a) and the aerosol number
296 concentration in the 15–50 nm range ($N_{15-50 \text{ nm}}$) increases sharply in the morning
297 almost every day (Fig. 2b). The time series of the mean diameter (D_m) of particles also
298 shows that a growth process occurs after the sharp increase in $N_{15-50 \text{ nm}}$. All these
299 phenomena suggest that new particle formation (NPF) events frequently occurred at
300 XT during the field experiment (Kulmala et al., 2012; Y. Li et al., 2017). This is likely
301 related to the high concentration of gas precursors from mainly local emissions. High
302 emissions of SO_2 and VOCs associated with the high oxidation capacity in a polluted
303 atmosphere make NPF events occur more frequently in northern China (Z. Wang et al.,
304 2017).

305 Figure 2c-d shows time series of the probability density functions (PDFs) of κ_{gf}
306 (κ -PDF) for 40-nm and 150-nm particles, respectively. In general, mono-modal
307 κ -PDFs were observed. This is different from κ -PDFs at other sites in China where
308 bi- and tri-modal distributions dominate (Liu et al., 2011; Ye et al., 2013; Jiang et al.,
309 2016; S. L. Zhang et al., 2016; Y. Wang et al., 2017). Differences in the aerosol
310 mixing state explain this (see section 4.2).

311 Figure 3a shows the bulk mass concentrations of organics, sulfate, nitrate,
312 ammonium, and chloride measured by the ACSM and the BC mass concentration

313 measured by the AE-33. Organics and sulfate were the dominant chemical species
314 with mass fractions in PM_{10} of 39.1% and 24.7%, respectively. Figure 3b-c shows the
315 volume fractions of paired chemical compositions and κ_{chem} , respectively. The average
316 volume fraction of inorganics ($(NH_4)_2SO_4+NH_4HSO_4+H_2SO_4+NH_4NO_3$) was similar
317 to that of organics (POA+SOA), but their volume fractions changed diurnally. In
318 general, the volume fraction of inorganics increased during daytime while the volume
319 fraction of organics decreased. SOA was the dominant contributor to OA, accounting
320 for ~69% of the organics volume. This shows that photochemical reactions were
321 strong at XT during the field campaign (Huang et al., 2014). The mean κ_{chem} in Fig.
322 3c was 0.31 with values ranging from 0.20 to 0.40. The trend in κ_{chem} was similar to
323 that of the volume fraction of inorganics. This suggests that inorganics played a key
324 role in κ_{chem} . This is consistent with the study by Wu et al. (2016).

325 **4.2. Aerosol mixing state and hygroscopicity**

326 Figure 4 shows mean κ -PDFs for different particle sizes derived from H-TDMA
327 data. For all particle sizes considered, κ_{gf} ranged from 0 to 0.8, and the κ -PDF
328 patterns were similar. This suggests that hygroscopic compounds in different particle
329 size modes were similar at XT. In general, κ -PDF patterns show only one hydrophilic
330 mode with a weak hydrophobic mode occasionally appearing at night when
331 photochemical reactions are weak (Fig. S4). The κ -PDF patterns always show bi- or
332 tri-modal distributions at other sites in China (Liu et al., 2011; Ye et al., 2013; Jiang et
333 al., 2016; Zhang et al., 2016; Y. Wang et al., 2017). Based on previous studies (Liu et

334 al., 2011; Y. Wang et al., 2017), ambient aerosols can be classified into three groups
335 according to their κ_{gf} values:

- 336 — nearly hydrophobic (NH): $\kappa_{gf} < 0.1$
- 337 — less hygroscopic (LH): $0.1 \leq \kappa_{gf} < 0.2$
- 338 — more hygroscopic (MH): $0.2 \leq \kappa_{gf}$

339 Table 1 gives the number fractions of each group for different particle sizes. The MH
340 group dominated all particle sizes. The number fractions of the NH and LH groups
341 were both less than 6.0%. However, the volume fractions of hydrophobic BC and
342 low-hygroscopic organics (where κ_{BC} is approximately zero and $\kappa_{organic}$ is
343 typically less than 0.1) were ~10.1% and 47.4%, respectively, according to chemical
344 composition measurements (Fig. 3b). This suggests that the particles were highly aged
345 and internally mixed at XT during the field campaign. The coating of sulfates and
346 secondary organics during the aging process changes the structure of BC and makes
347 these particles grow which can significantly enhance the hygroscopicities of particles
348 (e.g., Zhang et al., 2008; Jimenez et al., 2009; Tritscher et al., 2011; Guo et al., 2016).
349 The observed unimodal distribution of κ -PDF also suggests the internal mixing state
350 of the particles (Swietlicki et al., 2008).

351 Figure 5 shows the average size-resolved κ_{gf} derived from H-TDMA data at XT
352 and other sites in China. At XT, κ_{gf} for different particle sizes were larger in the
353 daytime than at night, and the difference between daytime and nighttime decreased
354 with increasing particle size. This suggests that the impact of photochemical reactions
355 on aerosol hygroscopicity is strong. The effect is weaker with increasing particle size

356 because most of the larger particles are always well aged.

357 The magnitude of κ_{gf} was larger at XT than at other sites in China. In particular,
358 the magnitude of κ_{gf} was much larger at XT than at sites in the northern part of the
359 NCP, i.e., Beijing, Wuqing, and Xianghe. The lower κ_{gf} in the Beijing urban area is
360 likely related to the more severe traffic emissions there (Ye et al., 2013; Wu et al.,
361 2016). Wuqing and Xianghe are located in the suburban area between the two
362 megacities of Beijing and Tianjin and are simultaneously affected by traffic and
363 industrial emissions. The magnitudes of κ_{gf} at these two sites are higher than at
364 Beijing but lower than at XT. Although distant from these megacities, XT is situated
365 in the industrial center of the NCP, so particles there are more internally mixed and
366 highly aged due to the higher concentrations of precursors and strong photochemical
367 reactions. This is why κ_{gf} at XT is larger than at other sites. This suggests that the
368 hygroscopicities of particles from different emissions and chemical processes differ in
369 the NCP. Forty nm particles were always more hygroscopic than 80-nm particles at
370 XT, especially in the daytime. This differed from other sites likely because the coating
371 effect of sulfates and secondary organics is more significant for smaller particles
372 (Tritscher et al., 2011; Guo et al., 2016). Furthermore, since the field measurements
373 took place in a locality with heavy industrial activities, it is possible that amine
374 contributed significantly to the hygroscopicity of 40-nm particles. Several studies
375 have shown that amine compounds in aerosol phase can be hygroscopic, sometimes at
376 even low RH (e.g., Qiu and Zhang, 2012; Chu et al., 2015; Gomez-Hernandez et al.,
377 2016).

378 **4.3. Diurnal variations in aerosol properties**

379 **4.3.1. Diurnal variations in aerosol number and mass concentrations**

380 Figure 6a shows the diurnal variation in MPL-derived PBL height. The PBL
381 height is the altitude where a sudden decrease in the MPL-measured scattering
382 coefficient occurs (Cohn and Angevine, 2000; Brooks, 2003). Note that the retrieved
383 PBL height is only valid from 0700 local time (LT) to 1900 LT (Quan et al., 2013).
384 The retrieved PBL height at night is not accurate because of the likely influence of
385 residual aerosols within the nocturnal PBL. The evolution of PBL height from 0700
386 LT to 1900 LT is sufficient to analyze its link with the change in aerosol number and
387 mass concentrations during the daytime. Figure 6b shows diurnal variations in aerosol
388 number and mass concentrations in the 15–685 nm range ($N_{15-685\text{ nm}}$ and $PM_{15-685\text{ nm}}$,
389 respectively). Variations in $N_{15-685\text{ nm}}$ and $PM_{15-685\text{ nm}}$ trended opposite from each other.
390 From 0800 LT to 1400 LT, the PBL height lifted from ~0.5 km to ~0.6 km, while
391 $PM_{15-685\text{ nm}}$ generally decreased from ~24 $\mu\text{g m}^{-3}$ to ~19 $\mu\text{g m}^{-3}$. This suggests the
392 important effect of PBL evolution on $PM_{15-685\text{ nm}}$. However, $N_{15-685\text{ nm}}$ sharply
393 increased from ~7600 cm^{-3} at 0700 LT to ~13,000 cm^{-3} at 1300 LT. This is related to
394 the sudden burst of small Aitken-mode particles (< 50 nm) during NPF events. Newly
395 formed fine particles contribute little to $PM_{15-685\text{ nm}}$. In the evening, $PM_{15-685\text{ nm}}$
396 increased gradually while $N_{15-685\text{ nm}}$ decreased. The decline of the nocturnal PBL and
397 particle coagulation and growth explains this. In other words, the evolution of the
398 PBL influenced the aerosol mass concentration, while particle formation and growth
399 had a greater influence on the variation in aerosol number concentration.

400 **4.3.2. Diurnal variation in aerosol hygroscopicity**

401 Figure 6c shows diurnal variations in κ_{gf} and κ_{chem} . Values of κ_{gf} for different
402 particle sizes increased in the morning when the NPF event started. The increase was
403 sharpest for 40-nm particles. The increase in κ_{gf} in the morning synchronized with
404 the particle number concentration ($N_{15-685 \text{ nm}}$) but not with the PBL height, further
405 suggesting the impact of photochemical reactions on aerosol hygroscopicity. The κ_{gf}
406 for 40-nm particles increased from ~ 0.32 at 0700 LT to ~ 0.44 at 1500 LT and
407 approached the κ value of pure ammonium sulfate. This also suggests that a large
408 amount of hygroscopic compounds were produced during NPF events. Fig. S5 shows
409 sharply increased concentrations of SO_2 and VOCs in the morning and the enhanced
410 atmospheric oxidation capacity under high RH and low T conditions. The production
411 of sulfate and SOAs resulted. This is why aerosol hygroscopicity and the occurrence
412 of NPF events increased. Zhang et al. (2018) characterized the aerosol chemistry
413 during NPF events in this field campaign. The diurnal pattern in κ_{gf} for 80–200 nm
414 particles differs from that of 40-nm particles. The differences in κ_{gf} for 80–200 nm
415 particles in the early morning were large but gradually decreased as the sun rose. The
416 κ_{gf} for 80–200-nm particles were similar but lower than that for 40-nm particles after
417 1100 LT. The condensation of sulfates and secondary organics likely caused the
418 enhanced hygroscopicity of the 40–200-nm particles, especially of 40-nm particles
419 (Fig. 6d).

420 Figure 6c also shows that the κ_{chem} for PM_{10} was lower than the κ_{gf} for 40–
421 200-nm particles and had a weaker diurnal variation. This feature was stronger at

422 noon when atmospheric oxidation and the aging process were more rapid. The simple
423 ZSR mixing rule is responsible for this. During the daytime, the condensation of
424 sulfuric acid on organics or BC greatly enhances their hygroscopicities (Zhang et al.,
425 2008; Zhang et al., 2017). The ZSR model cannot accurately represent this
426 phenomenon. Cruz and Pandis (2000) have shown that the measured κ_{gf} of internally
427 mixed $(\text{NH}_4)_2\text{SO}_4$ -organic aerosols is larger than the predicted κ_{chem} based on the
428 ZSR model.

429 In summary, the ample supply of SO_2 and VOCs provided sufficient precursors
430 for the strong photochemical reactions at XT during this field campaign, and the
431 production and condensation of sulfate and SOAs greatly enhanced aerosol
432 hygroscopicity, especially during the daytime. The oxidation of precursors likely
433 induced the observed frequent NPF events.

434 **4.3.3. Diurnal variation in CCN number concentration and activation ratio**

435 Figure 7a shows the diurnal variations in N_{CCN} and AR at different SS. In the
436 morning, N_{CCN} first decreased then increased while AR showed the opposite trend.
437 This is related to the evolution of the PBL and NPF events. At the initial stage of an
438 NPF event, the newly formed particles were less than 15 nm in size which was below
439 the detection limit of the SMPS. As a result, $N_{15-685 \text{ nm}}$ decreased (Fig. 6b) as the PBL
440 lifted, and N_{CCN} also decreased. However, the mixing of aged particles within the PBL
441 made the particle size (Fig. 7b) and AR increase slightly. Condensation and the
442 growth of new particles caused the number of fine particles detected by the SMPS to

443 increase rapidly. However, because of their smaller sizes, some of these particles were
444 not activated. Therefore, N_{CCN} increased, but AR decreased from 0800 LT to 1400 LT.
445 In the afternoon and evening, N_{CCN} and AR increased slightly as particle sizes
446 increased (Fig. 7b). These trends weakened as SS decreased because the critical
447 diameter is larger at low SS and the influence of aerosol size distribution on N_{CCN} and
448 AR is relatively weaker. Particle size was the most important factor influencing
449 aerosol activation and CCN number concentrations, especially at larger SS. Figure 6S
450 shows the results from a sensitivity test of particle size in a CCN closure study similar
451 to that done by Dusek et al. (2006).

452 **4.4. CCN estimation from chemical composition data**

453 This section presents a CCN closure study and a discussion of the impact of
454 chemical composition on N_{CCN} . It is reasonable to assume that aerosols are internally
455 mixed when estimating N_{CCN} because H-TDMA data showed that this was the case at
456 XT. Figure 8a shows estimated N_{CCN} as a function of measured N_{CCN} using real-time
457 κ_{chem} . The estimated N_{CCN} correlates well with measurements ($R^2 \geq 0.85$), but is
458 generally overestimated. The slope of each linearly fitted line is greater than 1.10 and
459 increases with increasing SS. The relative deviation (RD) increases from 16.2% to
460 25.2% as SS increases from 0.13% to 0.75%, suggesting that estimates become worse
461 at larger SS. The large measurement uncertainties of CCNC mainly cause the
462 overestimation of N_{CCN} : (1) The temperature or high flow rates in the CCNC may not
463 allow enough time for particles to reach sizes large enough to be counted by the

464 optical particle counter at the exit of the CCN chamber (Lance et al., 2006; Cubison et
465 al., 2008) and (2) in high particle number concentration environments, water depletion
466 in the CCNC may reduce the counting rate of the CCNC (Deng et al., 2011). These
467 uncertainties make measured N_{CCN} lower than the actual N_{CCN} . At larger SS, activated
468 aerosols in the cloud chamber of the CCNC are greater in number and smaller in size,
469 so the impact of these uncertainties is greater. Figure S7 shows results from the N_{CCN}
470 closure study for separated N_{CCN} . The CCN closure is reasonable when $N_{CCN} < 5500$
471 cm^{-3} .

472 Figure 8b shows estimated N_{CCN} using the mean value for κ_{chem} ($\kappa_{chem} = 0.31$).
473 Compared with results using real-time values for κ_{chem} , the fit parameters and RD
474 change slightly, suggesting that the effect of chemical composition on N_{CCN} is weaker
475 relative to the particle size. Figure 9 shows the sensitivity of estimated N_{CCN} to the
476 variability in chemical composition. The variability in the equipotential lines of RD
477 suggests that the sensitivity of N_{CCN} is strongly time dependent. This is attributed to
478 the variability of the shape of the aerosol size distribution (Juranyi et al., 2010) which
479 further demonstrates the importance of particle size to N_{CCN} . The sensitivity of N_{CCN}
480 to chemical composition (κ_{chem}) becomes weaker with increasing SS, suggesting that
481 chemical composition becomes less important in N_{CCN} estimates at larger SS. RD is
482 always less than 10% when estimating N_{CCN} using the mean value of κ_{chem} . The
483 value $\kappa = 0.31$ is thus a good reference value to model N_{CCN} in this region.

484 In summary, the particle size is the most important factor influencing aerosol
485 activation at XT, especially at larger SS. The chemical composition was not as

486 important when estimating N_{CCN} because particles were highly aged and internally
487 mixed at XT. Aerosol hygroscopicity was not sensitive to estimates of N_{CCN} .

488 **5. Summary and conclusions**

489 The Atmosphere-Aerosol-Boundary Layer-Cloud (A²BC) Interaction Joint
490 Experiment was done at a suburban site (Xingtai, or XT) located in the central North
491 China Plain (NCP) from 1 May to 15 June of 2016. The study investigated aerosol
492 hygroscopicity, the mixing state, and CCN activity at XT.

493 In general, the probability density function (PDF) of the hygroscopicity parameter
494 κ (κ -PDF) for 40–200-nm particles was a unimodal distribution, which is different
495 from distributions at other sites in China. Particles of all sizes covered a large range of
496 κ_{gf} (the hygroscopicity parameter derived from H-TDMA measurements; mostly
497 from 0 to 0.8) and showed similar κ -PDF patterns, suggesting that the hygroscopic
498 compounds in these particles from 40 nm to 200 nm were similar at XT. The κ -PDF
499 patterns also suggest that particles were highly aged and internally mixed at XT
500 during the field campaign. This is likely related to strong photochemical reactions.

501 The mean κ_{gf} for different particle sizes were larger in the daytime than at night.
502 Daytime and nighttime κ_{gf} differences decreased with increasing particle size. The
503 impact of photochemical reactions on aerosol hygroscopicity was strong, and the
504 effect became weaker as particle size increased. The coating of sulfates or secondary
505 organics likely enhanced the hygroscopicities of 40–200-nm particles. This effect was
506 more significant for 40-nm particles. Compared with other sites in China, the aerosol

507 hygroscopicity was much larger at XT because of the sufficient amount of precursors
508 and strong atmospheric oxidation. The comparison also shows that the
509 hygroscopicities of particles from different emissions and chemical processes differed
510 greatly.

511 New particle formation events occurred frequently at XT during this field
512 campaign. The evolution of the planetary boundary layer influenced the aerosol mass
513 concentration, while particle formation and growth had a greater influence on the
514 variation in aerosol number concentration. Particle size was the most important factor
515 influencing aerosol activation and the CCN number concentration (N_{CCN}) at XT,
516 especially at larger supersaturations (SS). Although estimated N_{CCN} correlated well
517 with measurements ($R^2 \geq 0.85$), N_{CCN} was overestimated because of measurement
518 uncertainties. The effect of chemical composition on N_{CCN} was weaker relative to the
519 particle size. Sensitivity tests show that the impact of chemical composition on N_{CCN}
520 became weaker as SS increased, suggesting that the effect of chemical composition on
521 the estimation of N_{CCN} is less important at larger SS. The value $\kappa = 0.31$ is a good
522 proxy for N_{CCN} in this region.

523 XT is located in the most polluted region in China. The multitude of factories in the
524 region generates strong emissions. The plenitude of gas precursors and strong
525 photochemical reactions at XT make aerosol properties there unique. More field
526 measurements on gas-particle transformation and aerosol properties in this region are
527 needed for studying haze formation mechanisms and climate effects.

528
529 *Data availability.* Data used in the study are available from the first author upon

530 request (wang.yuying@mail.bnu.edu.cn).

531

532 *Competing interests.* The authors declare that they have no conflict of interest.

533

534 *Author contribution.* Z. L. and Y. W. designed the experiment; Y. W., Y. Z., and W. D.
535 carried it out and analyzed the data; other co-authors participated in science discussions
536 and suggested analyses. Y. W. prepared the manuscript with contributions from all
537 co-authors.

538

539 *Acknowledgements.* This work was funded by National Natural Science Foundation of
540 China (NSFC) research projects (grant no. 91544217, 41675141, 41705125), the
541 National Basic Research Program of China “973” (grant no. 2013CB955801), and the
542 China Scholarship Council (award no. 201706040194). We thank all participants in
543 the field campaign for their tireless work and cooperation.

544

545 **References**

546 Albrecht, B. A.: Aerosols, cloud microphysics, and fractional cloudiness, *Science*, 245,
547 1227–1230, <https://doi.org/10.1126/science.245.4923.1227>, 1989.

548 Brooks, I. M.: Finding boundary layer top: application of a wavelet covariance
549 transform to lidar backscatter profiles, *J. Atmos. Ocean. Tech.*, 20, 1092–1105,
550 [https://doi.org/10.1175/1520-0426\(2003\)020<1092:FBLTAO>2.0.CO;2](https://doi.org/10.1175/1520-0426(2003)020<1092:FBLTAO>2.0.CO;2), 2003.

551 Chu, Y., Sauerwein, M., and Chan, C. K.: Hygroscopic and phase transition properties
552 of alkyl aminium sulfates at low relative humidities, *Phys. Chem. Chem. Phys.*, 17,
553 19,789–19,796, <https://doi.org/10.1039/c5cp02404h>, 2015.

554 Cohn, S. A., and Angevine, W. M.: Boundary layer height and entrainment zone
555 thickness measured by lidars and wind-profiling radars, *J. Appl. Meteorol.*, 39,
556 1233–1247,
557 [https://doi.org/10.1175/1520-0450\(2000\)039<1233:BLHAEZ>2.0.CO;2](https://doi.org/10.1175/1520-0450(2000)039<1233:BLHAEZ>2.0.CO;2), 2000.

558 Cruz, C. N., and Pandis, S. N.: Deliquescence and hygroscopic growth of mixed
559 inorganic–organic atmospheric aerosol, *Environ. Sci. Technol.*, 34, 4313–4319,
560 <https://doi.org/10.1021/es9907109>, 2000.

561 Cubison, M. J., Ervens, B., Feingold, G., Docherty, K. S., Ulbrich, I. M., Shields, L.,
562 Prather, K., Hering, S., and Jimenez, J. L.: The influence of chemical composition
563 and mixing state of Los Angeles urban aerosol on CCN number and cloud
564 properties, *Atmos. Chem. Phys.*, 8, 5649–5667,
565 <https://doi.org/10.5194/acp-8-5649-2008>, 2008. Deng, Z. Z., Ma, N., Liu, P. F., Xu,
566 W. Y., Zhao, C. S., Ran, L., Chen, J., Liang, Z., Liang, S., and Huang, M. Y.:
567 Size-resolved and bulk activation properties of aerosols in the North China Plain,
568 *Atmos. Chem. Phys.*, 11, 3835–3846, <https://doi.org/10.5194/acp-11-3835-2011>,
569 2011.

570 Dusek, U., Frank, G. P., Hildebrandt, L., Curtius, J., Schneider, J., Walter, S., Chand,

571 D., Drewnick, F., Hings, S., and Jung D.: Size matters more than chemistry for
572 cloud-nucleating ability of aerosol particles, *Science*, 312, 1375–1378,
573 <https://doi.org/10.1126/science.1125261>, 2006.

574 Eichler, H., Cheng, Y. F., Birmili, W., Nowak, A., Wiedensohler, A., Brüggemann, E.,
575 Gnauk, T., Herrmann, H., Althausen, D., and Ansmann, A.: Hygroscopic properties
576 and extinction of aerosol particles at ambient relative humidity in South-Eastern
577 China, *Atmos Environ*, 42, 6321–6334,
578 <https://doi.org/10.1016/j.atmosenv.2008.05.007>, 2008.

579 Ervens, B., Cubison, M., Andrews, E., Feingold, G., Ogren, J. A., Jimenez, J. L.,
580 DeCarlo, P., and Nenes, A.: Prediction of cloud condensation nucleus number
581 concentration using measurements of aerosol size distributions and composition and
582 light scattering enhancement due to humidity, *J. Geophys. Res.-Atmos.*, 112,
583 <https://doi.org/10.1029/2006JD007426>, 2007.

584 Fu, G. Q., Xu, W. Y., Yang, R. F., Li, J. B., and Zhao, C. S.: The distribution and
585 trends of fog and haze in the North China Plain over the past 30 years, *Atmos.*
586 *Chem. Phys.*, 14, 11949–11958, <https://doi.org/10.5194/acp-14-11949-2014>, 2014.

587 Gomez-Hernandez, M., McKeown, M., Secrest, J., Marrero-Ortiz, W., Lavi, A.,
588 Rudich, Y., Collins, D. R., and Zhang, R.: Hygroscopic characteristics of
589 alkylammonium carboxylate aerosols, *Environ. Sci. Technol.*, 50, 2292–2300,
590 <https://dx.doi.org/10.1021/acs.est.5b04691>, 2016.

591 Guo, S., Hu, M., Lin, Y., Gomez-Hernandez, M., Zamora, M. L., Peng, J., Collins, D.
592 R., and Zhang, R.: OH-Initiated oxidation of m-xylene on black carbon aging,
593 *Environ. Sci. Technol.*, 50, 8605–8612, <https://dx.doi.org/10.1021/acs.est.6b01272>,
594 2016.

595 Gysel, M., Crosier, J., Topping, D. O., Whitehead, J. D., Bower, K. N., Cubison, M. J.,
596 Williams, P. I., Flynn, M. J., McFiggans, G. B., and Coe, H.: Closure study between
597 chemical composition and hygroscopic growth of aerosol particles during TORCH2,
598 *Atmos. Chem. Phys.*, 7, 6131–6144, <https://doi.org/10.5194/acp-7-6131-2007>,
599 2007.

600 Huang, R., Zhang, Y., Bozzetti, C., Ho, K., Cao, J., Han, Y., Daellenbach, K. R.,
601 Slowik, J. G., Platt, S. M., Canonaco, F., Zotter, P., Wolf, R., Pieber, S. M., Brun,
602 E. A., Crippa, M., Ciarelli, G., Piazzalunga, A., Schwikowski, M., Abbazade, G.,
603 Schnelle-Kreis, J., Zimmermann, R., An, Z., Szidat, S., Baltensperger, U., Haddad, I.
604 E., and Prévôt, A. S. H.: High secondary aerosol contribution to particulate
605 pollution during haze events in China, *Nature*, 514, 218–222,
606 <https://doi.org/10.1038/nature13774>, 2014.

607 IPCC: Climate change 2013: Scientific basis, Fifth assessment of the
608 Intergovernmental Panel on Climate Change, Cambridge University Press, 2013.

609 Jacobson, M. C., Hansson, H. C., Noone, K. J., and Charlson, R. J.: Organic
610 atmospheric aerosols: review and state of the science, *Rev. Geophys.*, 38, 267–294,
611 <https://doi.org/10.1029/1998RG000045>, 2000.

612 Jiang, R. X., Tan, H. B., Tang, L. L., Cai, M. F., Yin, Y., Li, F., Liu, L., Xu, H. B.,
613 Chan, P. W., Deng, X. J., and Wu, D.: Comparison of aerosol hygroscopicity and
614 mixing state between winter and summer seasons in Pearl River Delta region, China,

615 Atmos. Res., 169, 160–170, <https://doi.org/10.1016/j.atmosres.2015.09.031>, 2016.

616 Jimenez, J. L., Canagaratna, M. R., Donahue, N. M., Prevot, A., Zhang, Q., Kroll, J.
617 H., DeCarlo, P. F., Allan, J. D., Coe, H., and Ng, N. L.: Evolution of organic
618 aerosols in the atmosphere, *Science*, 326, 1525–1529,
619 <https://doi.org/10.1126/science.1180353>, 2009.

620 Juranyi, Z., Gysel, M., Weingartner, E., DeCarlo, P. F., Kammermann, L., and
621 Baltensperger, U.: Measured and modelled cloud condensation nuclei number
622 concentration at the high alpine site Jungfraujoch, *Atmos. Chem. Phys.*, 10, 7891–
623 7906, <https://doi.org/10.5194/acp-10-7891-2010>, 2010.

624 Köhler, H.: The nucleus in and the growth of hygroscopic droplets, *T. Faraday Soc.*,
625 32, 1152–1161, <https://doi.org/10.1039/TF9363201152>, 1936.

626 Kulmala, M., Petäjä, T., Nieminen, T., Sipilä, M., Manninen, H. E., Lehtipalo, K., Dal
627 Maso, M., Aalto, P. P., Junninen, H., and Paasonen, P.: Measurement of the
628 nucleation of atmospheric aerosol particles, *Nat. Protoc.*, 7, 1651–1667,
629 <https://doi.org/10.1038/nprot.2012.091>, 2012.

630 Lance, S., Nenes, A., Medina, J., and Smith, J. N.: Mapping the operation of the DMT
631 continuous flow CCN counter, *Aerosol Sci. Tech.*, 40, 242–254,
632 <http://dx.doi.org/10.1080/02786820500543290>, 2006.

633 Lebo, Z. J., Shipway, B. J., Fan, J., Geresdi, I., Hill, A., Miltenberger, A., Morrison,
634 H., Rosenberg, P., Varble, A., and Xue, L.: Challenges for cloud modeling in the
635 context of aerosol-cloud-precipitation interactions, *B. Am. Meteorol. Soc.*,
636 <https://doi.org/10.1175/BAMS-D-16-0291.1>, 2017.

637 Li, Y., Zhang, F., Li, Z., Sun, L., Wang, Z., Li, P., Sun, Y., Ren, J., Wang, Y., Cribb,
638 M., and Yuan, C.: Influences of aerosol physiochemical properties and new particle
639 formation on CCN activity from observation at a suburban site of China, *Atmos.*
640 *Res.*, 188, 80–89, <https://doi.org/10.1016/j.atmosres.2017.01.009>, 2017.

641 Li, Z., Lau, W. K.-M., Ramanathan, V., Wu, G., Ding, Y., Manoj, M. G., Liu, J., Qian,
642 Y., Li, J., Zhou T., Fan, J., Rosenfeld, D., Ming, Y., Wang, Y., Huang, J., Wang, B.,
643 Xu, X., Lee, S.-S., Cribb, M., Zhang, F., Yang, X., Zhao, C., Takemura, T., Wang,
644 K., Xia, X., Yin, Y., Zhang, H., Guo, J., Zhai, P. M., Sugimoto, N., Babu, S. S., and
645 Brasseur, G. P.: Aerosol and monsoon climate interactions over Asia, *Rev.*
646 *Geophys.*, 54, 866–929, <https://doi.org/10.1002/2015RG000500>, 2016.

647 Li, Z., Daniel, R., and Fan, J. W.: Aerosols and their impact on radiation, clouds,
648 precipitation, and severe weather events, *Oxford Research Encyclopedias:*
649 *Environmental Science*, <https://doi.org/10.1093/acrefore/9780199389414.013.126>,
650 2017a.

651 Li, Z., Guo, J., Ding, a., Liao, h., Liu, J., Sun, Y., Wang, T., Xue, H., Zhang, H., and
652 Zhu, B.: Aerosols and boundary-layer interactions and impact on air quality, *Natl.*
653 *Sci. Rev.*, 4, 810–833, doi:10.1093/nsr/nwx117, 2017b.

654 Liu, P. F., Zhao, C. S., Bel, T. G., Hallbauer, E., Nowak, A., Ran, L., Xu, W. Y.,
655 Deng, Z. Z., Ma, N., Mildnerberger, K., Henning, S., Stratmann, F., and
656 Wiedensohler, A.: Hygroscopic properties of aerosol particles at high relative
657 humidity and their diurnal variations in the North China Plain, *Atmos. Chem. Phys.*,
658 11, 3479–3494, <https://doi.org/10.5194/acp-11-3479-2011>, 2011.

659 Lopez-Yglesias, X. F., Yeung, M. C., Dey, S. E., Brechtel, F. J., and Chan, C. K.:
660 Performance evaluation of the Brechtel Mfg. Humidified Tandem Differential
661 Mobility Analyzer (BMI HTDMA) for studying hygroscopic properties of aerosol
662 particles, *Aerosol Sci. Tech.*, 48, 969–980,
663 <http://dx.doi.org/10.1080/02786826.2014.952366>, 2014.

664 Meng, J. W., Yeung, M. C., Li, Y. J., Lee, B. Y. L., and Chan, C. K.: Size-resolved
665 cloud condensation nuclei (CCN) activity and closure analysis at the HKUST
666 Supersite in Hong Kong, *Atmos. Chem. Phys.*, 14, 10267–10282,
667 <https://doi.org/10.5194/acp-14-10267-2014>, 2014.

668 Ng, N. L., Herndon, S. C., Trimborn, A., Canagaratna, M. R., Croteau, P. L., Onasch,
669 T. B., Sueper, D., Worsnop, D. R., Zhang, Q., and Sun, Y. L.: An Aerosol Chemical
670 Speciation Monitor (ACSM) for routine monitoring of the composition and mass
671 concentrations of ambient aerosol, *Aerosol Sci. Tech.*, 45, 780–794,
672 <http://dx.doi.org/10.1080/02786826.2011.560211>, 2011.

673 Petters, M. D., and Kreidenweis, S. M.: A single parameter representation of
674 hygroscopic growth and cloud condensation nucleus activity, *Atmos. Chem. Phys.*,
675 7, 1961–1971, <https://doi.org/10.5194/acp-7-1961-2007>, 2007.

676 Qiu, C., and Zhang, R.: Physicochemical properties of alkylammonium sulfates:
677 hygroscopicity, thermostability, and density, *Environ. Sci. Technol.*, 46, 4474–4480,
678 <https://dx.doi.org/10.1021/es3004377>, 2012.

679 Quan, J., Gao, Y., Zhang, Q., Tie, X., Cao, J., Han, S., Meng, J., Chen, P., and Zhao,
680 D.: Evolution of planetary boundary layer under different weather conditions, and
681 its impact on aerosol concentrations, *Particuology*, 11, 34–40,
682 <https://doi.org/10.1016/j.partic.2012.04.005>, 2013.

683 Ramanathan, V., Crutzen, P. J., Kiehl, J. T., and Rosenfeld, D.: Aerosols, climate, and
684 the hydrological cycle, *Science*, 294, 2119–2124,
685 <https://doi.org/10.1126/science.1064034>, 2001.

686 Rose, D., Gunthe, S. S., Mikhailov, E., Frank, G. P., Dusek, U., Andreae, M. O., and
687 Pöschl, U.: Calibration and measurement uncertainties of a continuous-flow cloud
688 condensation nuclei counter (DMT-CCNC): CCN activation of ammonium sulfate
689 and sodium chloride aerosol particles in theory and experiment, *Atmos. Chem.*
690 *Phys.*, 8, 1153–1179, <https://doi.org/10.5194/acp-8-1153-2008>, 2008.

691 Rosenfeld, D., U. Lohmann, G. B. Raga, C. D. O'Dowd, M. Kulmala, S. Fuzzi, A.
692 Reissell, and M. O. Andreae, Flood or drought: How do aerosols affect
693 precipitation?, *Science*, 321, doi:10.1126/science.1160606, 2008.

694 Schmale, J., Henning, S., Decesari, S., Henzing, B., Keskinen, H., Sellegri, K.,
695 Ovadnevaite, J., Pöhlker, M. L., Brito, J., Bougiatioti, A., Kristensson, A., Kalivitis,
696 N., Stavroulas, I., Carbone, S., Jefferson, A., Park, M., Schlag, P., Iwamoto, Y.,
697 Aalto, P., Äijälä, M., Bukowiecki, N., Ehn, M., Frank, G., Fröhlich, R., Frumau, A.,
698 Herrmann, E., Herrmann, H., Holzinger, R., Kos, G., Kulmala, M., Mihalopoulos,
699 N., Nenes, A., O'Dowd, C., Petäjä, T., Picard, D., Pöhlker, C., Pöschl, U., Poulain,
700 L., Prévôt, A. S. H., Swietlicki, E., Andreae, M. O., Artaxo, P., Wiedensohler, A.,
701 Ogren, J., Matsuki, A., Yum, S. S., Stratmann, F., Baltensperger, U., and Gysel, M.:
702 Long-term cloud condensation nuclei number concentration, particle number size

703 distribution and chemical composition measurements at regionally representative
704 observatories, *Atmos Chem Phys*, 18, 2853–2881,
705 <https://doi.org/10.5194/acp-18-2853-2018>, 2018.

706 Stokes, R. H., and Robinson, R. A.: Interactions in aqueous nonelectrolyte solutions. I.
707 Solute-solvent equilibria, *J. Phys. Chem.*, 70, 2126–2131,
708 <https://doi.org/10.1021/j100879a010>, 1966.

709 Stolzenburg, M. R., and McMurry, P. H.: Equations governing single and tandem
710 DMA configurations and a new lognormal approximation to the transfer function,
711 *Aerosol Sci. Tech.*, 42, 421–432, <http://dx.doi.org/10.1080/02786820802157823>,
712 2008.

713 Stolzenburg, M. R., and McMurry, P. H.: TDMAFIT user’s manual, University of
714 Minnesota, Department of Mechanical Engineering, Particle Technology
715 Laboratory, Minneapolis, 1–61, 1988.

716 Sun, Y., Wang, Z., Dong, H., Yang, T., Li, J., Pan, X., Chen, P., and Jayne, J. T.:
717 Characterization of summer organic and inorganic aerosols in Beijing, China with
718 an Aerosol Chemical Speciation Monitor, *Atmos. Environ.*, 51, 250–259,
719 <https://doi.org/10.1016/j.atmosenv.2012.01.013>, 2012.

720 Swietlicki, E., Hansson, H. C., Hämeri, K., Svenningsson, B., Massling, A.,
721 McFiggans, G., McMurry, P. H., Petäjä, T., Tunved, P., Gysel, M., Topping, D.,
722 Weingartner, E., Baltensperger, U., Rissler, J., Wiedensohler, A., and Kulmala, M.:
723 Hygroscopic properties of submicrometer atmospheric aerosol particles measured
724 with H-TDMA instruments in various environments—a review, *Tellus B*, 60, 432–
725 469, <https://doi.org/10.1111/j.1600-0889.2008.00350.x>, 2008.

726 Tan, H., Xu, H., Wan, Q., Li, F., Deng, X., Chan, P. W., Xia, D., and Yin, Y.: Design
727 and application of an unattended multifunctional H-TDMA system, *J. Atmos.*
728 *Ocean. Tech.*, 30, 1136–1148, <https://doi.org/10.1175/JTECH-D-12-00129.1>, 2013.

729 Tritscher, T., Juranyi, Z., Martin, M., Chirico, R., Gysel, M., Heringa, M. F., DeCarlo,
730 P. F., Sierau, B., Prévôt, A. S. H., Weingartner, E., and Baltensperger, U.: Changes
731 of hygroscopicity and morphology during ageing of diesel soot, *Environ. Res. Lett.*,
732 6, <https://doi.org/10.1088/1748-9326/6/3/034026>, 2011.

733 Twomey, S.: Pollution and the planetary albedo, *Atmos. Environ.*, 8, 1251–1256,
734 [https://doi.org/10.1016/0004-6981\(74\)90004-3](https://doi.org/10.1016/0004-6981(74)90004-3), 1974.

735 Ulbrich, I. M., Canagaratna, M. R., Zhang, Q., Worsnop, D. R., and Jimenez, J. L.:
736 Interpretation of organic components from Positive Matrix Factorization of aerosol
737 mass spectrometric data, *Atmos. Chem. Phys.*, 9, 2891–2918,
738 <https://doi.org/10.5194/acp-9-2891-2009>, 2009.

739 Wang, L. T., Wei, Z., Yang, J., Zhang, Y., Zhang, F. F., Su, J., Meng, C. C., and
740 Zhang, Q.: The 2013 severe haze over the southern Hebei, China: model evaluation,
741 source apportionment, and policy implications, *Atmos. Chem. Phys. Disc.*, 13,
742 3151–3173, <https://doi.org/10.5194/acp-14-3151-2014>, 2014.

743 Wang, Y., Zhang, F., Li, Z., Tan, H., Xu, H., Ren, J., Zhao, J., Du, W., and Sun, Y.:
744 Enhanced hydrophobicity and volatility of submicron aerosols under severe
745 emission control conditions in Beijing, *Atmos. Chem. Phys.*, 17, 5239–5251,
746 <https://doi.org/10.5194/acp-17-5239-2017>, 2017.

747 Wang, Z., Wu, Z., Yue, D., Shang, D., Guo, S., Sun, J., Ding, A., Wang, L., Jiang, J.,
748 and Guo, H.: New particle formation in China: current knowledge and further
749 directions, *Sci. Total Environ.*, 577, 258–266,
750 <https://doi.org/10.1016/j.scitotenv.2016.10.177>, 2017.

751 Wu, Z. J., Zheng, J., Shang, D. J., Du, Z. F., Wu, Y. S., Zeng, L. M., Wiedensohler,
752 A., and Hu, M.: Particle hygroscopicity and its link to chemical composition in the
753 urban atmosphere of Beijing, China, during summertime, *Atmos. Chem. Phys.*, 16,
754 1123–1138, <https://doi.org/10.5194/acp-16-1123-2016>, 2016.

755 Ye, X., Tang, C., Yin, Z., Chen, J., Ma, Z., Kong, L., Yang, X., Gao, W., and Geng,
756 F.: Hygroscopic growth of urban aerosol particles during the 2009 Mirage-Shanghai
757 Campaign, *Atmos. Environ.*, 64, 263–269,
758 <https://doi.org/10.1016/j.atmosenv.2012.09.064>, 2013.

759 Zhang, F., Li, Y., Li, Z., Sun, L., Li, R., Zhao, C., Wang, P., Sun, Y., Liu, X., Li, J.,
760 Li, P., Ren, G., and Fan, T.: Aerosol hygroscopicity and cloud condensation nuclei
761 activity during the AC³Exp campaign: implications for cloud condensation nuclei
762 parameterization, *Atmos. Chem. Phys.*, 14, 13423–13437,
763 <https://doi.org/10.5194/acp-14-13423-2014>, 2014.

764 Zhang, F., Li, Z., Li, Y., Sun, Y., Wang, Z., Li, P., Sun, L., Wang, P., Cribb, M., Zhao,
765 C., Fan, T., Yang, X., and Wang, Q.: Impacts of organic aerosols and its oxidation
766 level on CCN activity from measurement at a suburban site in China, *Atmos. Chem.*
767 *Phys.*, 16, 5413–5425, <https://doi.org/10.5194/acp-16-5413-2016>, 2016.

768 Zhang, F., Wang, Y., Peng, J., Ren, J., Collins, D., Zhang, R., Sun, Y., Yang, X., and
769 Li, Z.: Uncertainty in predicting CCN activity of aged and primary aerosols, *J.*
770 *Geophys. Res.-Atmos.*, 122, <https://doi.org/10.1002/2017JD027058>, 2017.

771 Zhang, R., Khalizov, A. F., Pagels, J., Zhang, D., Xue, H., and McMurry, P. H.:
772 Variability in morphology, hygroscopicity, and optical properties of soot aerosols
773 during atmospheric processing, *P. Natl. Acad. Sci. USA*, 105, 10291–10296,
774 <https://doi.org/10.1073/pnas.0804860105>, 2008.

775 Zhang, S. L., Ma, N., Kecorius, S., Wang, P. C., Hu, M., Wang, Z. B., Größ, J., Wu, Z.
776 J., and Wiedensohler, A.: Mixing state of atmospheric particles over the North
777 China Plain, *Atmos. Environ.*, 125, Part A, 152–164,
778 <https://doi.org/10.1016/j.atmosenv.2015.10.053>, 2016. Zhang, Y., Du, W., Wang, Y.,
779 Wang, Q., Wang, H., Zheng, H., Zhang, F., Shi, H., Bian, Y., Han, Y., Fu, P.,
780 Canonaco, F., Prévôt, A. S. H., Zhu, T., Wang, P., Li, Z., and Sun, Y.: Aerosol
781 chemistry and particle growth events at an urban downwind site in the North China
782 Plain, *Atmos. Chem. Phys. Discuss.*, 2018, 1–29,
783 <https://doi.org/10.5194/acp-2017-889>, 2018.

784 Zhu, Y., Zhang, J., Wang, J., Chen, W., Han, Y., Ye, C., Li, Y., Liu, J., Zeng, L., Wu,
785 Y., Wang, X., Wang, W., Chen, J., and Zhu, T.: Distribution and sources of air
786 pollutants in the North China Plain based on on-road mobile measurements, *Atmos.*
787 *Chem. Phys.*, 16, 12551–12565, <https://doi.org/10.5194/acp-16-12551-2016>, 2016.

788
789
790

791
792
793
794
795
796
797

Table 1. Number fractions of different hygroscopic groups for different particle sizes.

	40 nm	80 nm	110 nm	150 nm	200 nm
NH	5.1 %	5.0 %	5.1 %	5.0 %	5.7 %
LH	4.8 %	4.2 %	4.3 %	4.7 %	5.1 %
MH	90.1 %	90.8 %	90.6 %	90.3 %	89.2 %

NH: nearly hydrophobic; LH: less hygroscopic; MH: more hygroscopic

798
799
800
801

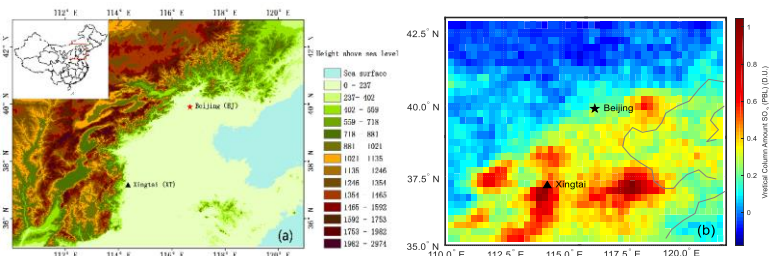


Figure 2. (a) Map showing the location of the sampling site and (b) the distribution of mean SO_2 concentrations from May of 2012 to 2016.

802
803
804
805

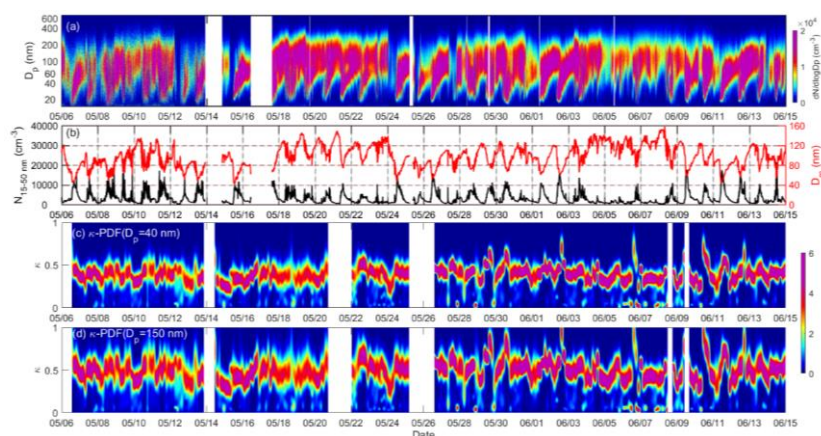
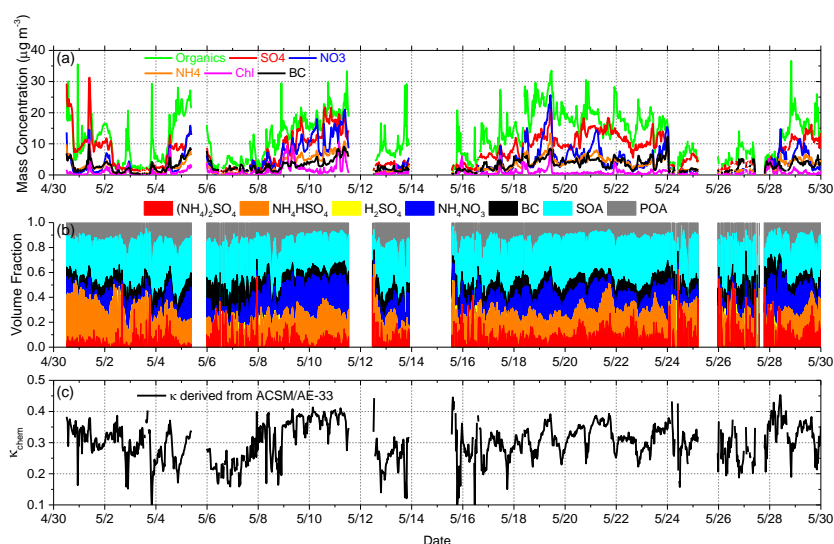


Figure 3. The time series of (a) the particle number size distribution, (b) the aerosol number concentration in the 15–50 nm range ($N_{15-50 \text{ nm}}$) and the geometric mean diameter (D_m), (c) the probability density function of κ_{gf} for 40-nm and (d) 150-nm

806 particles from 6 May to 15 June of 2016.

807
808



809

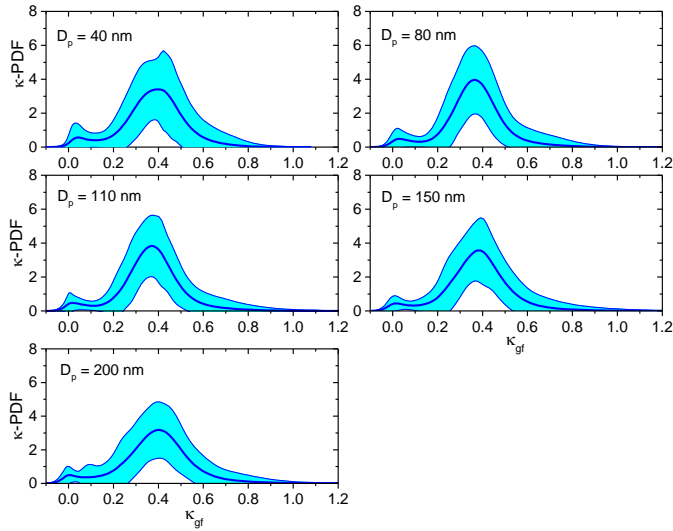
810 **Figure 4.** Time series of (a) the bulk mass concentration of aerosol species in PM_{10} , (b)

811 the volume fractions of POA, SOA, BC, and inorganics with the simplified

812 ion-pairing scheme, and (c) the hygroscopicity parameter derived from the chemical

813 composition (κ_{chem}).

814



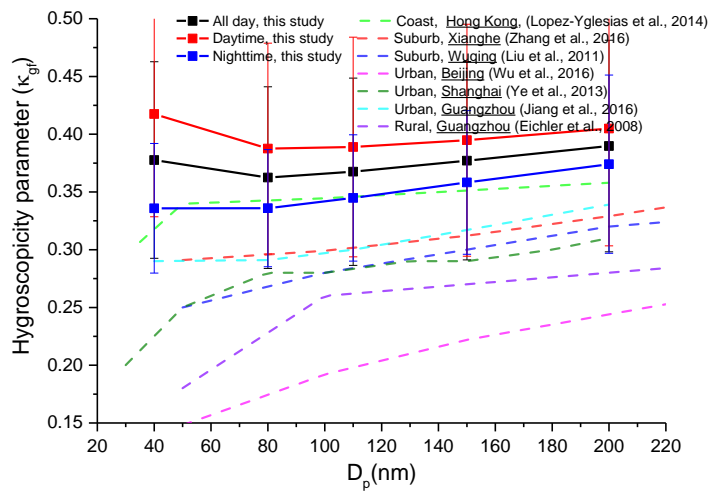
815

816 **Figure 5.** Mean probability density functions of κ_{gf} (κ -PDF) for different particle

817 sizes and their standard deviations (shaded areas) derived from H-TDMA data and

818 measured at RH = 85 %.

819

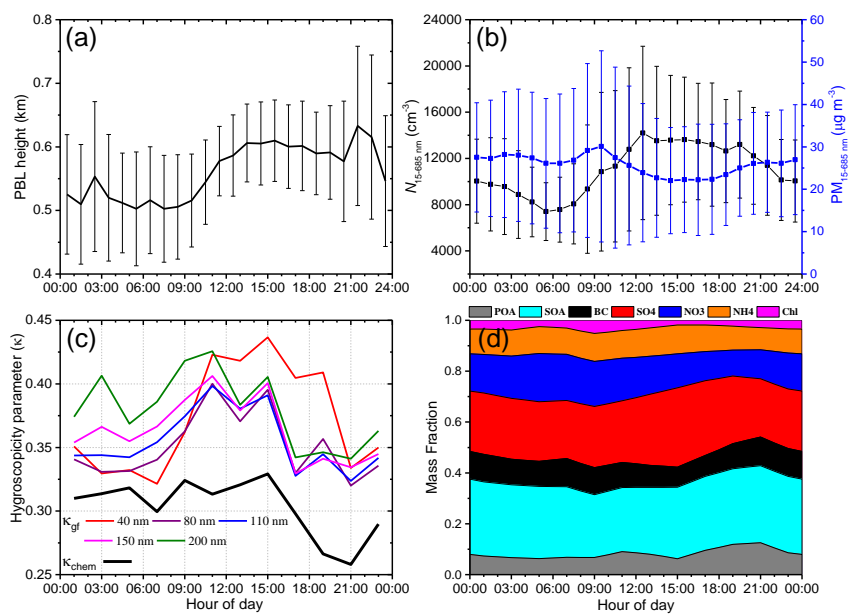


820

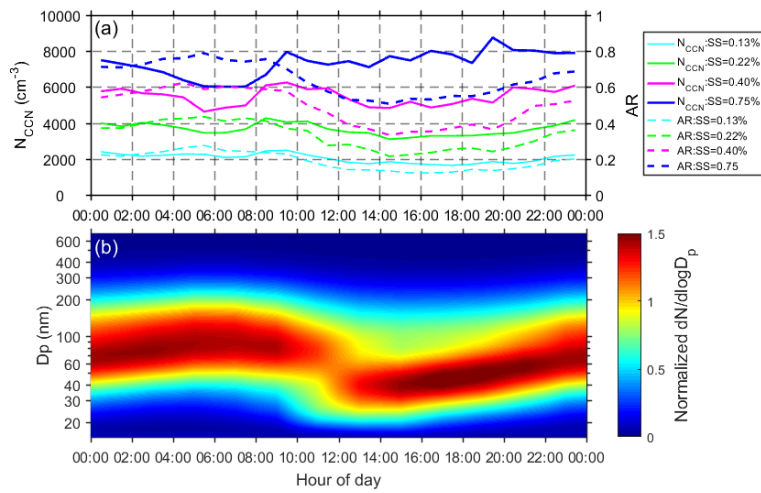
821 **Figure 6.** Size-resolved aerosol hygroscopicity parameter derived from H-TDMA

822 data at XT and at other sites in China.

823



824
 825 **Figure 7.** Diurnal variations in (a) planetary boundary layer (PBL) height retrieved
 826 from micropulse lidar data, (b) aerosol number and mass concentrations in the 15–685
 827 nm range ($N_{15-685\text{ nm}}$ and $\text{PM}_{15-685\text{ nm}}$, respectively) derived from the SMPS (an aerosol
 828 density of 1.6 g cm^{-3} is assumed), (c) the hygroscopicity parameter derived from the
 829 hygroscopic growth factor (κ_{gf}) and predicted from the bulk chemical composition
 830 (κ_{chem}), and (d) the mass fractions of different species.
 831



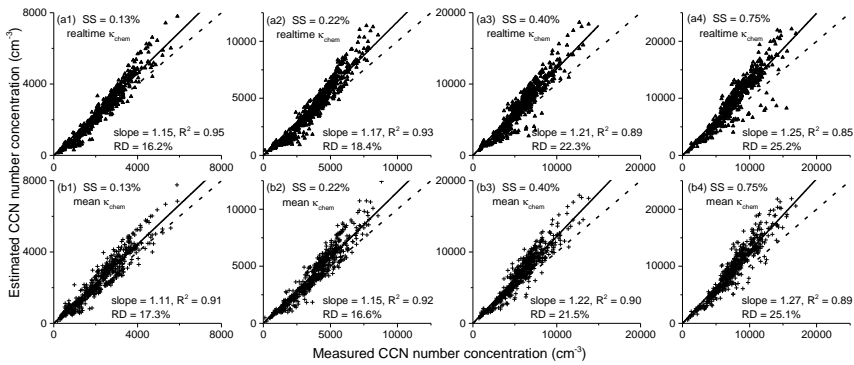
832

833 **Figure 8.** Diurnal variations in (a) CCN number concentration (N_{CCN}) and activation

834 ratio (AR), and (b) the normalized aerosol size distribution in the 15–685-nm particle

835 size range.

836



837

838

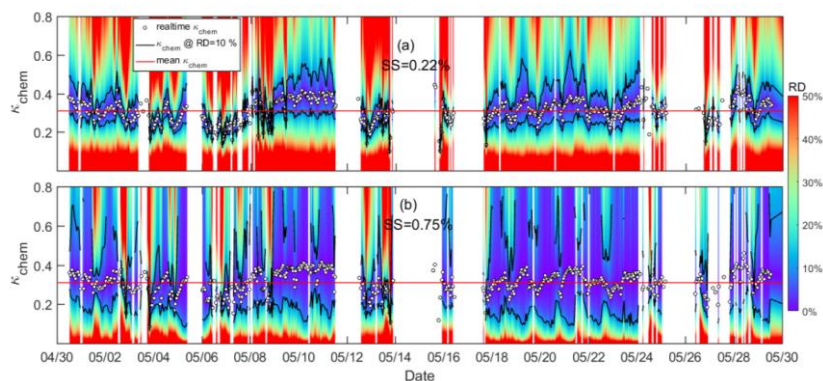
839 **Figure 9.** Estimated versus measured cloud condensation nuclei (CCN) number

840 concentrations (N_{CCN}) for ambient aerosols at four different supersaturation (SS)

841 levels. The N_{CCN} is estimated based on κ -Köhler theory using the real-time κ_{chem}

842 (a1-a4) and the mean κ_{chem} (b1-b4). The slope and coefficient of determination (R^2)

843 of the linear regression and the relative deviation (RD) of estimated N_{CCN} (RD =
 844 $|N_{CCN_estimated} - N_{CCN_measured}| / N_{CCN_measured}$) are shown in each panel. The regression
 845 line is overlaid on the measurements (solid line) and the dashed line is the 1:1 line.
 846
 847



848
 849 **Figure 10.** Sensitivity of N_{CCN} estimates to κ_{chem} as a function of time at (a) SS =
 850 0.22% and (b) SS = 0.75%. The color scale indicates the relative deviation (RD) of
 851 CCN estimates using the κ_{chem} value shown on the ordinate. In each panel, open
 852 circles show the real-time κ_{chem} . Note that RD is by definition zero at these points.
 853 The black line is κ at RD = 10% and the red line is the mean value for κ_{chem} (0.31).
 854 Figure S8 in the supplement shows the same plots but for SS = 0.13% and 0.40%.

855
 856